Tuning three-dimensional higher-order topological insulators by surface state hybridization

Hao-Jie Lin [1,*], Hai-Peng Sun [2], Tianyu Liu,[1,3] and Peng-Lu Zhao [4,†]

[1]*Shenzhen Institute for Quantum Science and Engineering and Department of Physics,*
Southern University of Science and Technology (SUSTech), Shenzhen 518055, China
[2]*Institute for Theoretical Physics and Astrophysics, University of Würzburg, 97074 Würzburg, Germany*
[3]*International Quantum Academy, Shenzhen 518048, China*
[4]*Department of Physics, University of Science and Technology of China, Hefei 230026, Anhui, China*

Higher-order topological insulators (HOTIs) are a novel class of materials that exhibit exotic boundary states. The finite size effect induced hybridization between the boundary state HOTIs, however, remains largely unexplored. In this work, we analytically and numerically study the hybridization in films of three-dimensional chiral second-order topological insulators (SOTIs). We show that the gaps of two gapped surfaces (Chern insulators) are increased upon reducing the film thickness to a finite value. Meanwhile, in the presence of the hybridization of chiral edge states, we find that the gapless chiral hinge states (i.e., the boundary states of the surface Chern insulators) can be gapped, destroying the SOTIs. Moreover, we show that the gapless surfaces would in general be gapped due to the hybridization of surface states for a finite-sized system. Our work demonstrates that HOTIs exhibit a rich variety of physics under the influence of finite-size effects.

I. INTRODUCTION

Higher-order topological materials, exemplified by higher-order topological insulators (HOTIs), emerge as a novel direction in the studies of topological matter [1–30]. In contrast to the d-dimensional topological insulators (TIs) [31–40] which exhibit topologically protected gapless states on the $(d-1)$-dimensional boundaries, d-dimensional HOTIs host gapped $(d-1)$-dimensional boundaries but are characterized by gapless boundary states in dimensions even lower. For instance, a three-dimensional (3D) second-order topological insulator (SOTI) has gapped 2D surfaces but harbors gapless 1D hinge states. The experimental implementations of HOTIs are reported in acoustic [41–43] and photonic [44–47] metamaterials as well as electric circuits [48,49], while theories have proposed $CrI_3/Bi_2Se_3/MnBi_2Se_4$ heterostructures [50], $MnBi_{2n}Te_{3n+1}$ [51,52], $EuIn_2As_2$ [53], $EuSn_2As_2$ [54], and Sm-doped Bi_2Se_3 [55] to be chiral HOTIs.

The finite-size effect is known to have drastic impacts on topological matter [40,56–64]. For 2D TIs like the HgTe/CdTe quantum well [40,56], the size in the out-of-plane (i.e., stacking) direction can serve as a tuning parameter for topology. This is because the quantum well undergoes an inversion and experiences a topological phase transition when the thickness of the HgTe layer is tuned to a certain threshold. On the other hand, reducing the size in the in-plane direction of the HgTe/CdTe quantum well retains the bulk gap but allows hybridization of the helical edge states [57], which then become fully gapped. Similar finite-size effects akin to

2D TIs are also anticipated in 3D TIs [58,59,64,65]. When tuning a 3D TI into a thin film, the bulk gap remains intact. However, the Dirac surface states at the top and bottom of the film can cross the film and hybridize with each other. As a result, the Dirac surface states become gapped, and this Dirac gap exhibits remarkable oscillations with changes in the film thickness [65]. Since the 3D TI thin film [65] can be described using the Bernevig-Hughes-Zhang model [40] originally developed for the 2D HgTe/CdTe quantum well with thickness-dependent parameters, we can reinterpret the variation in the surface gap of the 3D TI as a corresponding variation in the bulk gap of the HgTe/CdTe quantum well. This reinterpretation helps to illustrate the previously mentioned topological phase transition that occurs when adjusting the thickness of the HgTe layer. In addition to 2D and 3D TIs, the finite-size effects have also been investigated in topological semimetals [61,62]. Reducing the thickness of 3D topological Dirac semimetals to a few layers in 2D leads to the gapping of 2D bulk energy bands, and gives rise to a quantum spin Hall phase [61]. Similarly, magnetic Weyl semimetals can also exhibit the emergence of a quantum anomalous Hall phase when undergoing a dimensional crossover [62]. However, a systematic investigation of the finite-size effects in HOTIs remains an uncharted territory. It remains unclear whether decreasing the sample size will bolster the stability of HOTIs or unveil new phases, and the fate of gapless hinge states is also still unknown.

In this work, we present a systematic analysis of the finite-size effect in 3D chiral SOTIs. To start with, we show that in an infinite-sized system, the gapped surfaces of a chiral SOTI effectively behave like Chern insulators, carrying gapless hinge states. Next, we demonstrate that when subjected to the finite-size effect, the Chern insulating surface states undergo a

---

*linhj2020@mail.sustech.edu.cn
†zhaoplu@gmail.com

process of hybridization. Importantly, this hybridization does not fundamentally alter the inherent nature of the surface states as Chern insulators but rather results in an increase in the surface Chern gap. This observation stands in stark contrast to the behavior in typical TIs, where hybridization alters the nature of the surface states, leading to the originally gapless Dirac states acquiring a gap. Furthermore, we clarify that the hybridization of hinge states has the potential to induce a gap in these states. Lastly, we demonstrate that the gapless surfaces of the SOTIs in general become gapped because of the hybridization of the surface Dirac states.

The paper is organized as follows. In Sec. II, we derive the effective model for the gapped surfaces of the infinite-sized chiral SOTIs and characterize the surface topology with a quantized anomalous Hall conductance. The next sections are about finite-size effects. In Sec. III, the surface energy gap is derived for a film of SOTIs. In Sec. IV, we investigate the behaviors of the hinge states. In Sec. V, we derive an effective model for the gapless surfaces of the SOTIs and obtain the surface energy gaps. Section VI concludes the paper and discusses several topics related to our work.

II. EFFECTIVE SURFACE HAMILTONIAN

To study the finite-size effect in 3D chiral SOTIs, we start from the following tight-binding model [5],

$$\hat{H}_L(\boldsymbol{k}) = \left(M_L + t \sum_i \cos k_i a\right)\tau_z\sigma_0 + \Delta_1 \sum_i \sin k_i a\ \tau_x\sigma_i$$
$$+ \Delta_2(\cos k_x a - \cos k_y a)\tau_y\sigma_0, \quad (1)$$

where a is the lattice constant, $i = x, y, z$, τ_i and σ_i are Pauli matrices for orbital and spin degrees of freedom, respectively, and M_L, t, Δ_1, and Δ_2 are model parameters. A SOTI is found in the regime $1 < |M_L/t| < 3$ and $\Delta_1, \Delta_2 \neq 0$. The term proportional to Δ_2 arises from the orbital currents. Both the time-reversal symmetry $\hat{T} = \tau_0\sigma_y\hat{K}$ and the fourfold rotation symmetry $\hat{C}_{4z} = \tau_0 e^{-i\frac{\pi}{4}\sigma_z}$ are broken as (see the Supplemental Material [66], Sec. SI, for details)

$$\hat{T}\hat{H}_L(\boldsymbol{k})\hat{T}^\dagger = \hat{H}_L(-\boldsymbol{k}) - 2\Delta_2(\cos k_x a - \cos k_y a)\tau_y\sigma_0 \quad (2)$$

and

$$\hat{C}_{4z}\hat{H}_L(\boldsymbol{k})\hat{C}_{4z}^\dagger = \hat{H}_L(-k_y, k_x, k_z)$$
$$+ 2\Delta_2(\cos k_x a - \cos k_y a)\tau_y\sigma_0. \quad (3)$$

The combined symmetry $\hat{C}_{4z}\hat{T}$ persists. This $\hat{C}_{4z}\hat{T}$ symmetry allows characterizing the chiral SOTIs with a $\mathbb{Z}_2$ index [12], thus being analogous to the time-reversal symmetry for TIs.

An effective model can be obtained by expanding the tight-binding model $\hat{H}_L$ in the vicinity of the Γ point up to the order of k^2. Explicitly, it reads

$$\hat{H}(\boldsymbol{k}) = (M - Bk_x^2)\gamma_0 + v\sum_i k_i\gamma_i - D(k_x^2 - k_y^2)\gamma_5, \quad (4)$$

where $\gamma_0 = \tau_z\sigma_0$, $\gamma_5 = \tau_y\sigma_0$, $\gamma_i = \tau_x\sigma_i$ $(i = x, y, z)$ are Dirac gamma matrices, $M = m - Bk^2$ with $m = M_L + 3t$, $k^2 = k_y^2 + k_z^2$, and $B = ta^2/2$, and $v = \Delta_1 a$, $D = \Delta_2 a^2/2$. For $D = 0$, the model Eq. (4) is reduced to a 3D TI. When D is finite, the energy bands of both (100) and (010) surfaces are gapped

while the (001) surface is gapless. The D term, which breaks the time-reversal symmetry, acts as an additional mass term and results in opposite effective masses for (100) and (010) surfaces. It thus leads to chiral hinge modes between these surfaces.

A. Effective model for surface states

First, we consider a semi-infinite SOTI that is confined along the x direction but periodic along the y and z directions. Following the approach in Refs. [65,67–69], the trial wave function associated with Eq. (4) can be written as (see Sec. SII of the Supplemental Material [66])

$$\psi_i(x, y, z) = \phi_i e^{\lambda x} e^{ik_y y} e^{ik_z z}. \quad (5)$$

Note that k_y and k_z are still good quantum numbers. Starting from the Schrödinger equation for the system, we obtain the secular equation

$$\det |\hat{H}(-i\lambda, k_y, k_z) - E| = 0, \quad (6)$$

which gives four doubly degenerate solutions marked as $\beta\lambda_\sigma$ with $\beta = \pm$, $\sigma = 1, 2$, and

$$\lambda_\sigma = \left[\frac{K_1 + (-1)^\sigma\sqrt{K_1^2 - K_2}}{2(B^2 + D^2)}\right]^{1/2}, \quad (7)$$

where $K_1 = v^2 - 2BM - 2D^2k_y^2$ and $K_2 = -4(B^2 + D^2)(M^2 - E^2 + v^2k^2 + D^2k_y^4)$. Because of the double degeneracy, each of the four $\beta\lambda_\sigma$ corresponds to two linearly independent four-component vectors

$$\psi_{\beta\sigma\gamma} = \begin{bmatrix} iv(k_y + \beta\lambda_\sigma) \\ vk_z + iD(k_y^2 + \lambda_\sigma^2) \\ 0 \\ \xi_\sigma \end{bmatrix}, \begin{bmatrix} iD(k_y^2 + \lambda_\sigma^2) - vk_z \\ -iv(k_y - \beta\lambda_\sigma) \\ \xi_\sigma \\ 0 \end{bmatrix}, \quad (8)$$

where $\gamma = 1, 2$ and $\xi_\sigma = M + B\lambda_\sigma^2 - E$. The general wave functions of the surface states $\Psi(x, k_y, k_z, E)$, excluding the plane wave solution part, are constructed by linearly superposing the trial wave functions as

$$\Psi(x, k_y, k_z, E) = \sum_{\beta=\pm} \sum_{\sigma,\gamma=1,2} C_{\beta\sigma\gamma}\psi_{\beta\sigma\gamma} e^{\beta\lambda_\sigma x}, \quad (9)$$

where $C_{\beta\sigma\gamma}$ are the superposition coefficients and determined by the boundary condition.

For the (100) and ($\bar{1}$00) surfaces, the boundary condition requires that $\Psi(x = 0, k_y, k_z, E) = 0$ and $\Psi(x \to \infty, k_y, k_z, E) = 0$, respectively. In general, we need these two boundary conditions to determine the general wave functions. However, for a semi-infinite system, the two parallel surfaces are independent of each other; we can focus on one surface and use one boundary condition to obtained the surface model and energy gap at such surface. As shown in Fig. 1(a), the surface states are localized near the surface and only penetrate into the bulk at the level of characteristic length $1/|\lambda_\sigma|$ as the solutions of the surface states have the form of $e^{-\lambda_\sigma x}$ with $\mathrm{Re}(\lambda_\sigma) > 0$. The wave functions on two parallel surfaces thus have negligible overlap for large thickness $L = 40$, and as
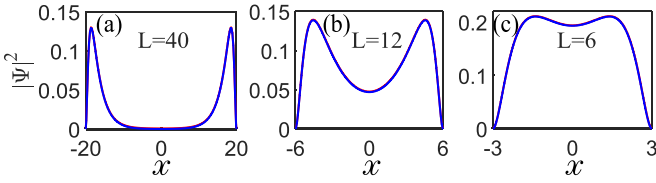
FIG. 1. Probability distributions of a chiral SOTI films of different thicknesses, illustrating the crossover from a 3D crystal to a 2D thin film. (a) The 3D geometry: For sufficiently thick slabs, probability is peaked at the boundaries while it exponentially decays into the bulk, indicating surface states localized at $x = \pm L/2$. (b) The quasi-2D geometry: Reducing the thickness, the surface states begin to overlap across the bulk but nonzero real part of λ. (c) The 2D geometry: For very small thickness, the surface states of the 3D crystal hybridize and eventually turn into the bulk states of the 2D thin film marked by $\mathrm{Re}\{\lambda\} = 0$.

a result, the two parallel surfaces are almost independent of each other. However, as shown in Fig. 1(b) and Fig. 1(c), when the thickness becomes smaller and smaller and finally dives into a 2D system, the wave function overlap becomes more and more important. To found the general solutions of the wave function for this system, one needs two boundary conditions.

For the semi-infinite system, we focus only the (100) surface and the boundary condition $\Psi(x = 0, k_y, k_z, E) = 0$ leads to (Sec. SI of the Supplemental Material [66])

$$\left\{B^2 v^2 k^2 + \left[BD k_y^2 - (M - E)D\right]^2\right\}(\lambda_1 + \lambda_2)^2$$
$$- \left[vB\lambda_1\lambda_2 - v(M - E)\right]^2 = 0. \tag{10}$$

Combining this equation with Eq. (7) yields the spectrum of the surface states, which is given by

$$E_{\pm} = \pm\frac{\sqrt{\left(Bk_y^2 - M\right)^2 D^2 + k^2 v^2(B^2 + D^2)}}{\sqrt{B^2 + D^2}}. \tag{11}$$

Note that when $D = 0$, the SOTIs turn into TIs. The energy dispersion $E_{\pm}$ transforms into $\pm vk$, signifying the emergence of a Dirac cone.

At the Γ point ($k_y = k_z = 0$), the wave functions of the surface state take the form

$$\psi_{\pm}(x) = C_{\pm}\begin{bmatrix} -\zeta_{\mp} \\ \pm\zeta_{\mp} \\ \mp 1 \\ 1 \end{bmatrix}(e^{-\lambda_1' x} - e^{-\lambda_2' x}), \tag{12}$$

where $C_{\pm}$ are the normalization factors and $\zeta_{\pm} = iB/(\sqrt{B^2 + D^2} \pm D)$. The solutions of the surface states on the opposite surface can be derived by applying the symmetry operator $\hat{I}\hat{T} = \tau_z\sigma_y\hat{K}$ to $\psi_{\pm}(x)$. The effective surface model can be obtained by projecting the bulk Hamiltonian onto the surface basis $(\psi_+, \psi_-)^T$ [65], which is given by

$$\hat{H}_{\mathrm{yz}} = v(\sigma_x k_y - \sigma_y k_z) + \frac{D[m - B(2k_y^2 + k_z^2)]}{\sqrt{B^2 + D^2}}\sigma_z. \tag{13}$$

For $D = 0$, the effective surface model becomes $\hat{H}_{\mathrm{yz}} = v(\sigma_x k_y - \sigma_y k_z)$, which corresponds to the surface model of a semi-infinite TI. When D is finite, the last term in Eq. (13)

acts as an effective mass, leading to a sizable energy gap for the surface states.

B. Topological property of surface states

Equation (13) is akin to a modified Dirac model that is commonly regarded as the effective model for describing Chern insulators [70]. To ensure that it correctly describes a Chern insulator, we will now investigate the topology of these surface states by evaluating the Berry curvature and the associated Hall conductivity. Equation (13) can be rewritten as $\hat{H}_{\mathrm{yz}} = d_0 + \boldsymbol{d}\cdot\boldsymbol{\sigma}$, where σ_i are the Pauli matrices, $d_0 = 0$, $d_x = vk_y$, $d_y = -vk_z$, $d_z = D[m - B(2k_y^2 + k_z^2)]/\sqrt{B^2 + D^2}$, and $d = \sqrt{d_x^2 + d_y^2 + d_z^2}$. The Berry curvature then reads

$$\Omega^x = \mp\frac{(\partial_{k_y}\boldsymbol{d} \times \partial_{k_z}\boldsymbol{d})\cdot\boldsymbol{d}}{2d^3}, \tag{14}$$

where the plus and minus signs are for the conduction band and the valence band, respectively [65,71]. For the valence band, the Berry curvature is (see Sec. SIIIB of the Supplemental Material [66])

$$\Omega^x = \frac{v^2 m'_+}{2(v^2 k^2 + m'^2_-)^{\frac{3}{2}}}, \tag{15}$$

where $m'_{\pm} = m' \pm B'(k^2 + k_y^2)$ and $m' = mD/\sqrt{B^2 + D^2}$, $B' = BD/\sqrt{B^2 + D^2}$. The corresponding Hall conductivity can be worked out via

$$\sigma_{yz} = \frac{e^2}{\hbar}\int\frac{d^2 k}{(2\pi)^2}(f_{k,v} - f_{k,c})\Omega^x(k). \tag{16}$$

At zero temperature, when the Fermi level lies in the surface gap, the quantized anomalous Hall conductivity reads

$$\sigma_{yz} = \frac{e^2}{h}\frac{\mathrm{sgn}(D)}{2}[\mathrm{sgn}(B) + \mathrm{sgn}(m)]. \tag{17}$$

The quantized anomalous Hall conductance depends on the sign of D. When focusing on the low-energy physics in the vicinity of the Γ point, the Hall conductance of the effective surface model [Eq. (13)] could be halved if discarding the $\mathrm{sgn}(BD)$ term, since it is from k reaching infinity. Equation (17) and its $\hat{C}_{4z}\hat{T}$ partner, which characterizes the opposite surface, allow us to introduce a $\mathbb{Z}_2$ index for the SOTI in consideration.

III. HYBRIDIZATION-ENHANCED SURFACE ENERGY GAP

In this section, we consider a slab of a SOTI to study the hybridization of the surface states. The slab is confined along the x direction with $x \in [-L/2, L/2]$ and still remains infinitely long along the y and z directions. The boundary conditions now become $\Psi(x = \pm L/2, k_y, k_z, E) = 0$. We then obtain a transcendental equation (see Sec. SIV of the Supplemental Material [66])

$$\frac{v^2\left(\lambda_1^2 + \lambda_2^2\xi^2\right) - D^2\left(\lambda_1^2 - \lambda_2^2\xi\right)^2}{v^2\lambda_1\lambda_2\xi} = \sum_{i\neq j}\frac{\tanh\left(\frac{\lambda_i L}{2}\right)}{\tanh\left(\frac{\lambda_j L}{2}\right)}, \tag{18}$$

where $i, j = 1, 2$, $\xi_i = (m - E + B\lambda_i^2)$, and $\xi = \xi_1/\xi_2$. The energies $E = E_{\pm}$ can be obtained by solving Eq. (18). The
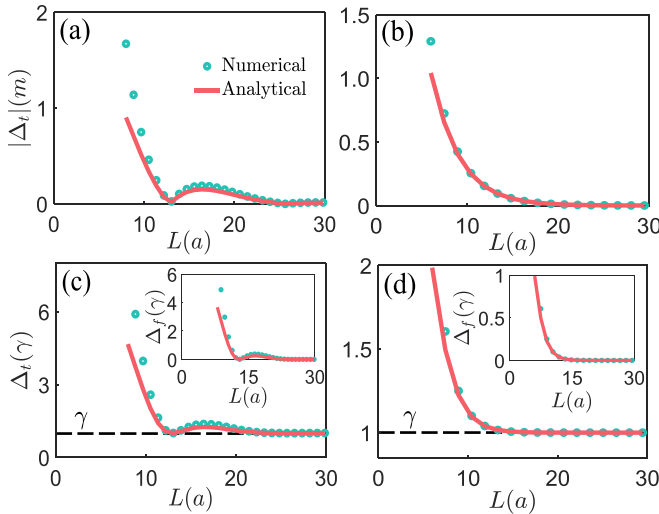
FIG. 2. The thickness L dependence of the surface energy gap Δ_t. (a) The surface energy gap of a TI in the parameter regime: $\lambda_{1,2} = a_\lambda \pm ib_\lambda$, $v = 0.8ta$, $B = 2.0ta^2$, $m = 0.2t$, and $D = 0$. Here, t is the hopping strength, and a is the lattice constant. (c) The surface energy gap of the SOTI for the same parameters of TI case except for $D = 0.2ta^2$. (b), (d) are the same as (a), (c), respectively, except that we set $\lambda_2 \gg \lambda_1$ and $B = 0.6ta^2$. In (c), (d), the dashed lines mark the surface gaps of infinitely sized SOTI, $\gamma = 2mD/\sqrt{B^2 + D^2}$, and the inset diagrams show the finite-sized gaps defined as $\Delta_f = \Delta_t - \gamma$. For all diagrams, the blue dots are obtained by numerically solving Eq. (18), and the red lines are approximate results for the same parameters.

energy gap illustrated in Fig. 2 is defined as $\Delta_t = E_+ - E_-$, which is measured with respect to the bulk gap in Fig. 2(a) and Fig. 2(c). To obtain a more analytically tractable expression for the energy gap, we will consider two cases that allow us to derive approximate analytical results. On the one hand, for generic (i.e., complex) $\lambda_{1,2} = a_\lambda \pm ib_\lambda$, where a_λ and b_λ are real quantities, the energy gap of surface states is given by

$$\Delta_t \approx 2m\sqrt{\frac{R_1 + R_2 + R_3}{(B^2 + D^2)(4Bm - v^2)^2}}, \quad (19)$$

where $R_1 = D^2(4Bm - v^2)^2$, $R_2 = 16B^2v^4(4Bm - v^2)\sin^2 (b_\lambda L)e^{-2a_\lambda L}$, and $R_3 = -64B^2v^4 \sin^4(b_\lambda L)e^{-4a_\lambda L}$. They possess different exponential attenuation behaviours to the thickness respectively. On the other hand, for real $\lambda_{1,2}$, if L is finite and the characteristic length satisfies $\lambda_2 \gg \lambda_1$, it is legitimate to write $\tanh(\lambda_2 L/2) \approx 1$. Consequently, the approximate energy gap of surface states reads

$$\Delta_t \approx 2m\sqrt{\frac{F_1 + F_2 + F_3}{(B^2 + D^2)(v^2 - 4Bm)^2}}, \quad (20)$$

where $F_1 = -4B^2v^4e^{-4\lambda_1'L}$, $F_2 = 4B^2v^2(v^2 - 4Bm)e^{-2\lambda_1'L}$, $F_3 = D^2(v^2 - 4Bm)^2$, and $\lambda_{1,2}'$ represent $\lambda_{1,2}$ at the Γ point.

The surface energy gap Δ_t can be divided into two parts: (i) the surface energy gap of an infinitely sized SOTI, $\gamma = 2mD/\sqrt{B^2 + D^2}$, which can be straightforwardly derived from the effective surface model [Eq. (13)], and (ii) the finite-sized effect induced gap $\Delta_f = \Delta_t - \gamma$ arising from the

overlap of the surfaces states that are located on opposite surfaces of the slab. Setting $D = 0$, the surface energy gap of a finite TI slab is acquired. We have shown the dependence of surface gap Δ_t on L in Figs. 2(a) and 2(c) for $\lambda_{1,2} = a_\lambda \pm ib_\lambda$ and $\lambda_2 \gg \lambda_1$, respectively. It is worth noting that such a gap is entirely induced by the finite-size effect because $\Delta_t \to 0$ as $L \to \infty$, which also indicates that the surface states of an infinitely sized TI are gapless Dirac fermions. As shown in Figs. 2(b) and 2(d), the SOTIs exhibit a gap-thickness relation similar to that of the TIs. The only difference is that for a sufficiently thick SOTI, the surface states exhibit a gap of size γ. The inset diagrams in Figs. 2(b) and 2(d) show the behaviors of $\Delta_f = \Delta_t - \gamma$, which approaches zero for $L \to \infty$. We thus conclude that the finite-size effects enhance the surface energy gap.

Reducing from the dimension of the SOTIs causes a crossover from a 3D to a 2D system. During this process, the hybridization of surface states results in a variable surface gap with respect to the thickness. For a TI, this gap makes the originally gapless Dirac surface acquire a gap, qualitatively altering the behavior of surface states. However, for HOTIs, which originally possess a surface gap, this increased gap does not qualitatively change the properties of surface states.

While we have understood the behavior of the surface state gap with respect to changes in the length, to further study the surface states, we will calculate their effective model. Because of the $\hat{I}\hat{T}$ symmetry, the eigenvectors corresponding to $E_\pm$ are doubly degenerate and take the forms (see Sec. SIV of the Supplemental Material [66])

$$\Psi_u^\pm(x) = C_u^\pm \begin{bmatrix} u_1^\pm f_- \\ u_2^\pm f_+ \\ -\tau_2^\pm \xi_1^\pm f_- \\ \xi_1^\pm f_+ \end{bmatrix}, \quad \Psi_d^\pm(x) = C_d^\pm \begin{bmatrix} u_3^\pm f_+ \\ u_4^\pm f_- \\ -\tau_1^\pm \xi_1^\pm f_+ \\ \xi_1^\pm f_- \end{bmatrix}. \quad (21)$$

To simplify the main text, we placed the expressions for $C_{u,d}^\pm$, $u_{1,2,3,4}^\pm$, $\tau_{1,2}^\pm$, $\xi_1^\pm$, and $f_\pm$ in Sec. SV of the Supplemental Material [66]. For a finite-sized system, $u_{1,2,3,4}^\pm$, $\tau_{1,2}^\pm$, and $f_\pm$ are dependent on L. In the basis $(\Psi_u^+, \Psi_u^-, \Psi_d^+, \Psi_d^-)^T$, the effective film Hamiltonian for real $\lambda_{1,2}$ can be derived through the projection approach outlined in Sec. II A as

$$\hat{H}_{yz}^L = (\Delta/2 - B_1 k^2 + D_1 k_y^2)\sigma_0\tau_z + v_1 k_y \sigma_x \tau_x + v_1 k_z \sigma_0 \tau_y + (D_2 k_y^2 - B_2 k^2)\sigma_z \tau_x, \quad (22)$$

where $B_1 = B\langle\Psi_u^+|\gamma_0|\Psi_u^+\rangle$, $B_2 = B\langle\Psi_u^+|\gamma_0|\Psi_u^-\rangle$, $D_1 = D \langle\Psi_u^+|\gamma_5|\Psi_u^+\rangle$, $D_2 = D\langle\Psi_u^+|\gamma_5|\Psi_u^-\rangle$, and $v_1 = v\langle\Psi_u^+|\gamma_y |\Psi_d^-\rangle$. The thickness dependencies of these parameters are illustrated in Figs. 3(a) to 3(e). The finite-size effects play important roles in tuning the coefficients of the quadratic terms. In the large-L limit, $D_2, B_2 \to 0$ [Figs. 3(c) and 3(d), respectively], $B_1, D_1 \to \pm BD/\sqrt{B^2 + D^2}$ [Figs. 3(b) and 3(e), respectively], and $\Delta \to 2mD/\sqrt{B^2 + D^2}$ [Fig. 3(f)]. As a result, the finite-sized Hamiltonian Eq. (22) recovers the dispersion relations in Eq. (11) with double degeneracy. Such a degeneracy can thus be understood as a combination of Eq. (11) and its $\hat{I}\hat{T}$ partner at the $(\bar{1}00)$ surface. Note that Eq. (22) is still a modified Dirac model. Furthermore,
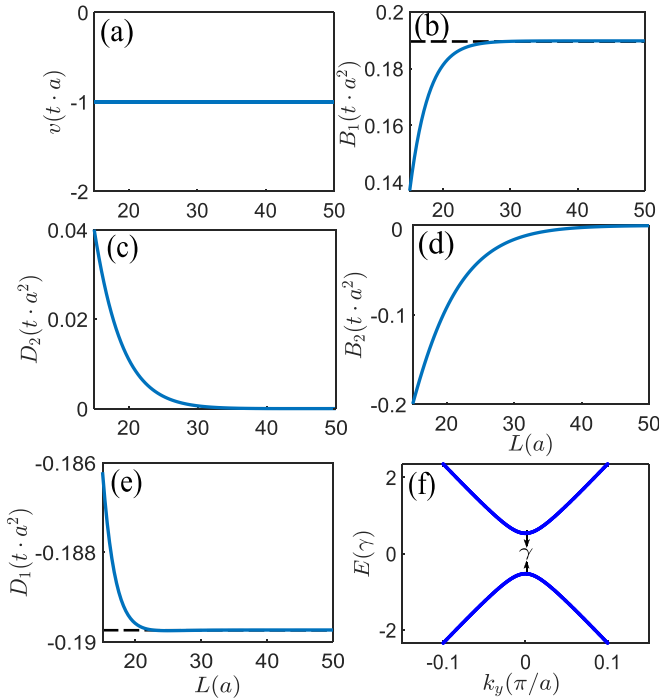
FIG. 3. (a)–(e) The dependence of the parameters v_1, B_1, B_2, D_1, and D_2 in Eq. (22) on the film thickness L. (f) The energy bands of the film in the large-thickness limit. The dashed black lines in (b) and (e) are $\pm BD/\sqrt{B^2 + D^2}$, respectively. For all diagrams, we set $m = 0.2t$, $B = 0.6ta^2$, $v = 1.0ta$, and $D = 0.2ta^2$.

considering that it could recover Eq. (11) in the large L, we thus conclude that Eq. (22) still describes a Chern insulator. The key difference is that the band parameters for such Chern insulators are highly dependent on the system size L. For complex $\lambda_{1,2}$, the effective model is provided in Sec. SV of the Supplemental Material [66], which shares the same conclusions.

IV. HINGE MODES UNDER HYBRIDIZATION

With finite-size effects, previous studies have revealed that the hybridization of edge states gives rise to rich phenomena in different topological systems. The quantum spin Hall insulators show mixed edge states, and as a result, the edge states have a gap [57]. Nonetheless, the edge states of quantum Hall insulators are independent of each other no matter how close they are [72–74], and the chiral edge states are always gapless. The underlying reason is that only two states with similar energy and momentum could couple together, leading to an energy gap when their wave functions overlap in real space [57]. Based on this argument, we think the edge states of a SOTI should be gapped when the size is small enough. Our numerical solutions of the band dispersion for the edge states confirm this conclusion.

We have numerically investigated the size effect on the hinge modes, and the results are presented in Fig. 4. As the system length decreases, the energy gap of the surface states increases, while the hinge modes become gapped. Specifically, as depicted in Fig. 4, for a relatively large length ($L = 20a$, shown by the blue line), the hinge states remain gapless.
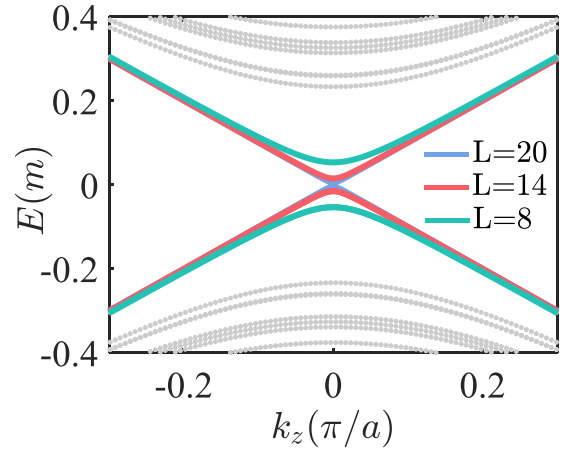

FIG. 4. The dashed lines represent the bulk and surface bands, while the colored bands represent the hinge modes. The hinge modes gap out as the length decreases. The parameters used in this picture are $v = 1.0ta$, $B = 0.5ta^2$, $m = 1.0t$, and $D = 0.1ta^2$.

However, as the length decreases (illustrated by the other two lines), the hinge modes become gapped, ultimately leading to the disruption of the HOTI phase.

To summarize, we have investigated the behavior of the (100) surface and its associated hinge states under finite-size effects. We have found that the effective theory describing the surface is consistently a modified Dirac Hamiltonian [70] with nontrivial topological properties. Notably, all the parameters within this Dirac Hamiltonian are significantly influenced by the system's size; especially, the surface gap is enhanced. Moreover, we have shown that the gapless hinge states become gapped. All these conclusions are established for the (010) surfaces because they are the $\hat{C}_{4z}\hat{T}$ partners of (100) surfaces.

V. HYBRIDIZATION ACROSS THE END SURFACES

In this section, we turn to investigate the finite-size effect of the (001) surface states and show that the gapless surface states in general become gapped. We consider a slab with open boundaries at $z = \pm L/2$, extending infinitely along the x and y directions. After applying a rotation to the Hamiltonian (see Sec. SVIC of the Supplemental Material [66]), we obtain a block-diagonal Hamiltonian near the Γ point with $k_x = k_y = 0$, given by

$$H_0 = \begin{bmatrix} h_0(v) & 0 \\ 0 & h_0(-v) \end{bmatrix}, \tag{23}$$

where $h_0(v) = (m + B\partial_z^2)\sigma_z - iv\partial_z\sigma_x$. The surface energy gap is determined by the eigenvalues of H_0. For its upper diagonal block $h_0(v)$, we utilize a trial eigenvector $(p_1, p_2)^T e^{\lambda z}$ and find that the corresponding eigenvalue problem leads to the following secular equation,

$$\begin{vmatrix} m + B\lambda^2 - E & -iv\lambda \\ -iv\lambda & -(m + B\lambda^2 + E) \end{vmatrix} = 0. \tag{24}$$

This equation leads to four λ values labeled as $\beta\lambda_\sigma$ with $\beta = \pm$ and $\sigma = 1, 2$. In terms of E and other model parameters,
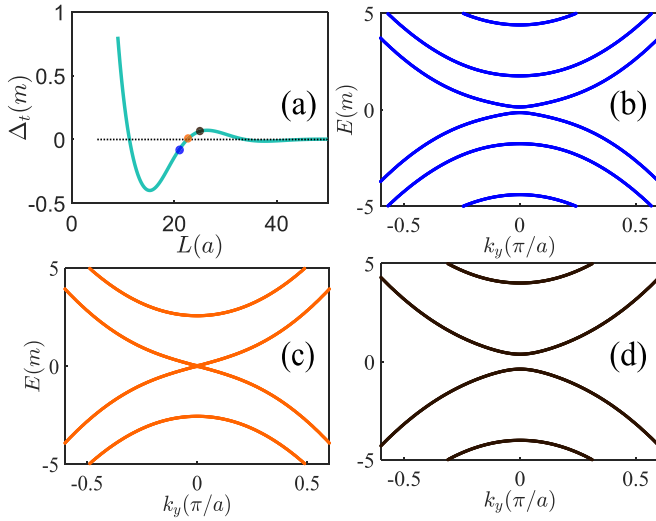
FIG. 5. (a) Dependence of the (001) surface gap on system length L. (b)–(d) The band structures for blue, red, and black points in (a), respectively. The parameters chosen are $D = 0.2ta^2$, $B = 2.0ta^2$, $v = 0.6ta$, and $m = 0.2t$.

λ_σ can be expressed as

$$\lambda_\sigma = \sqrt{\frac{v^2 - 2Bm}{2B^2}} \sqrt{1 + (-1)^\sigma \sqrt{1 + \frac{4B^2(E^2 - m^2)}{(v^2 - 2Bm)^2}}}, \quad (25)$$

which exhibits an E^2 dependence. The eigenvector of $h_0(v)$ can be constructed by the linear superposition of the trial eigenvectors associated with different $\beta\lambda_\sigma$ values by

$$\Psi(z) = \sum_{\beta = \pm} \sum_{\sigma = 1,2} C_{\beta\sigma} \begin{bmatrix} m + B\lambda_\sigma^2 + E \\ -iv\lambda \end{bmatrix} e^{\beta\lambda_\sigma z}. \quad (26)$$

Making the wave function conform to the boundary conditions, i.e., $\Psi(z = \pm L/2) = 0$, we find that the eigenvalues satisfy the following two transcendental equations:

$$\frac{m + B\lambda_1^2 + E}{m + B\lambda_2^2 + E} \frac{\lambda_2}{\lambda_1} = \frac{\tanh\left(\frac{\lambda_1 L}{2}\right)}{\tanh\left(\frac{\lambda_2 L}{2}\right)}, \quad (27)$$

$$\frac{m + B\lambda_1^2 + E}{m + B\lambda_2^2 + E} \frac{\lambda_2}{\lambda_1} = \frac{\tanh\left(\frac{\lambda_2 L}{2}\right)}{\tanh\left(\frac{\lambda_1 L}{2}\right)}. \quad (28)$$

These equations yield the eigenvalues $E_\pm$, from which the surface gap $\Delta_t = E_+ - E_-$ can be determined. We have numerically solved these equations and observed the dependence of the surface gap Δ on the thickness L. As shown in Figs. 5(a) to 5(d), when the thickness along the (001) direction is decreased, the surface gap begins to vary, and is gapped in general. Moreover, the (001) surface gap approaches zero for $L \to \infty$, confirming the conclusion that the (001) surface states are gapless for such a SOTI.

We now calculate the effective model for the (001) surfaces. With the solved eigenvalues $E_\pm$, the corresponding eigenvectors of $h_0(v)$ are given by

$$\Psi_\pm(z) = \tilde{C}_\pm \begin{bmatrix} B\eta^\pm f_\mp \\ -ivf_\pm \end{bmatrix}, \quad (29)$$

where $\tilde{C}_\pm$ are the normalization constants and

$$f_+ = \frac{\cosh(\lambda_1 z)}{\cosh(\lambda_1 L/2)} - \frac{\cosh(\lambda_1 z)}{\cosh(\lambda_1 L/2)},$$

$$f_- = \frac{\sinh(\lambda_1 z)}{\sinh(\lambda_1 L/2)} - \frac{\sinh(\lambda_1 z)}{\sinh(\lambda_1 L/2)},$$

$$\eta^+ = \frac{\lambda_2^2 - \lambda_1^2}{\lambda_2 \coth(\lambda_2 L/2) - \lambda_1 \coth(\lambda_1 L/2)}, \quad (30)$$

$$\eta^- = \frac{\lambda_2^2 - \lambda_1^2}{\lambda_2 \tanh(\lambda_2 L/2) - \lambda_1 \tanh(\lambda_1 L/2)}.$$

For simplification, we denote $\varphi_\pm(v) = \Psi_\pm(z)$; the four eigenvectors of H_0 [Eq. (23)] then can be rewritten as

$$\chi_1 = \begin{bmatrix} \varphi_+(v) \\ 0 \end{bmatrix}, \quad \chi_2 = \begin{bmatrix} 0 \\ \varphi_-(-v) \end{bmatrix},$$

$$\chi_3 = \begin{bmatrix} \varphi_-(v) \\ 0 \end{bmatrix}, \quad \chi_4 = \begin{bmatrix} 0 \\ \varphi_+(-v) \end{bmatrix}. \quad (31)$$

By projecting the full rotated bulk Hamiltonian $H = H_0 + \Delta H$, where $\Delta H = -Bk_\perp^2 \tau_0\sigma_z + v(k_x\tau_x\sigma_x + k_y\tau_y\sigma_x) - D(k_x^2 - k_y^2)\tau_0\sigma_y$ with $k_\perp^2 = k_x^2 + k_y^2$, onto the surface Hilbert space spanned by $[\chi_1, \chi_2, \chi_3, \chi_4]^T$, we obtained an effective Hamiltonian for the (001) surface,

$$\hat{H}_{xy}^L = -B_2 k_\perp^2 + (\Delta/2 - B_1 k_\perp^2)\sigma_z\tau_z$$
$$- D_1(k_x^2 - k_y^2)\sigma_x\tau_z - (k_x\sigma_0\tau_y - k_y\sigma_0\tau_x), \quad (32)$$

where

$$B_1 = \frac{B}{2}[\langle\varphi_+(v)|\sigma_z|\varphi_+(v)\rangle - \langle\varphi_-(-v)|\sigma_z|\varphi_-(-v)\rangle],$$

$$B_2 = \frac{B}{2}[\langle\varphi_+(v)|\sigma_z|\varphi_+(v)\rangle + \langle\varphi_-(-v)|\sigma_z|\varphi_-(-v)\rangle], \quad (33)$$

$$v_1 = v|\langle\varphi_+(v)|\sigma_x|\varphi_-(-v)\rangle|,$$

$$D_1 = D\langle\varphi_+(v)|\sigma_y|\varphi_-(v)\rangle.$$

In the absence of the term related to higher-order topology (i.e., $D = 0$), $\hat{H}_{\text{eff}}$ describes the surface states of a finite-sized 3D TI. We mention that such a term does not contribute to the surface gap because it is proportional to $k_x^2 - k_y^2$ and thus vanishes at the surface Γ point.

VI. CONCLUSIONS AND DISCUSSION

We present a comprehensive analysis of the finite-size effect in chiral SOTIs. For a semi-infinite SOTI, we find that the higher-order relevant D term, which distinguishes the SOTI from its TI counterparts, renders the (100) and (010) surfaces Chern insulators. For a film of a SOTI, we elucidated that the finite size effect induced hybridization between the two parallel surfaces results in enhanced surface energy gaps, which change with the film thickness. We show that the finite-size effect can gap out the chiral hinge states, which destroys the HOTI phase. Moreover, we demonstrate that the hybridization between the (001) and (00$\bar{1}$) surfaces generally results in energy gaps on both of these surfaces. It has been proposed that CrI$_3$/Bi$_2$Se$_3$/MnBi$_2$Se$_4$ heterostruc-

tures [50], MnBi$_{2n}$Te$_{3n+1}$ [51,52], EuIn$_2$As$_2$ [53], EuSn$_2$As$_2$ [54], and Sm-doped Bi$_2$Se$_3$ [55] are candidate chiral HOTI materials. We look forward to our theoretical predictions of the finite-size effects being tested in one or more of the above-mentioned materials. Furthermore, our results can be extended to two other closely related types of HOTIs. One type is HOTIs with all gapped surfaces, as introduced in [9]. We believe that finite-size effects will enhance the gap on every surface in such a model, ultimately gapping the edge states presented in [9]. The second type is HOTIs with helical edge states, primarily introduced in [5]. When subjected to finite-size effects, this type will exhibit the same behaviors as the chiral HOTIs considered in our work.

Our projection method can in principle be closely related to higher-order topological semimetals [75–83] to resolve their surface states and hinge Fermi arcs. Moreover, our numerical techniques solving the surface/hinge energy gaps allows us to check whether finite-size effects can induce topological phase transitions between the higher-order topological insulating and semimetallic phases. External electric and magnetic fields provide extra tuning knobs to the surface and hinge states of higher-order topological insulators [84,85]. It thus would be interesting to study the interplay between the finite-size effect and electromagnetic fields in higher-order topological semimetals.

[1] W. A. Benalcazar, B. A. Bernevig, and T. L. Hughes, Quantized electric multipole insulators, Science **357**, 61 (2017).

[2] W. A. Benalcazar, B. A. Bernevig, and T. L. Hughes, Electric multipole moments, topological multipole moment pumping, and chiral hinge states in crystalline insulators, Phys. Rev. B **96**, 245115 (2017).

[3] P.-L. Zhao, X.-B. Qiang, H.-Z. Lu, and X. C. Xie, Coulomb instabilities of a three-dimensional higher-order topological insulator, Phys. Rev. Lett. **127**, 176601 (2021).

[4] Z. Song, Z. Fang, and C. Fang, $(d-2)$-dimensional edge states of rotation symmetry protected topological states, Phys. Rev. Lett. **119**, 246402 (2017).

[5] F. Schindler, A. M. Cook, M. G. Vergniory, Z. Wang, S. S. P. Parkin, B. A. Bernevig, and T. Neupert, Higher-order topological insulators, Sci. Adv. **4**, eaat0346 (2018).

[6] F. Schindler, Z. Wang, M. G. Vergniory, A. M. Cook, A. Murani, S. Sengupta, A. Y. Kasumov, R. Deblock, S. Jeon, I. Drozdov *et al.*, Higher-order topology in bismuth, Nat. Phys. **14**, 918 (2018).

[7] C. M. Wang, H.-P. Sun, H.-Z. Lu, and X. C. Xie, 3D quantum Hall effect of Fermi arcs in topological semimetals, Phys. Rev. Lett. **119**, 136806 (2017).

[8] R. Chen, T. Liu, C. M. Wang, H.-Z. Lu, and X. C. Xie, Field-tunable one-sided higher-order topological hinge states in Dirac semimetals, Phys. Rev. Lett. **127**, 066801 (2021).

[9] B. Fu, Z.-A. Hu, and S.-Q. Shen, Bulk-hinge correspondence and three-dimensional quantum anomalous Hall effect in second-order topological insulators, Phys. Rev. Res. **3**, 033177 (2021).

[10] O. Pozo, C. Repellin, and A. G. Grushin, Quantization in chiral higher order topological insulators: Circular dichroism and local Chern marker, Phys. Rev. Lett. **123**, 247401 (2019).

[11] M. Di Liberto, N. Goldman, and G. Palumbo, Non-Abelian Bloch oscillations in higher-order topological insulators, Nat. Commun. **11**, 5942 (2020).

[12] H. Li and K. Sun, Pfaffian formalism for higher-order topological insulators, Phys. Rev. Lett. **124**, 036401 (2020).

[13] L. Fu, Topological crystalline insulators, Phys. Rev. Lett. **106**, 106802 (2011).

[14] K. Kudo, T. Yoshida, and Y. Hatsugai, Higher-order topological Mott insulators, Phys. Rev. Lett. **123**, 196402 (2019).

[15] C.-A. Li, S.-B. Zhang, J. C. Budich, and B. Trauzettel, Transition from metal to higher-order topological insulator driven by random flux, Phys. Rev. B **106**, L081410 (2022).

[16] M. J. Park, Y. Kim, G. Y. Cho, and S. B. Lee, Higher-order topological insulator in twisted bilayer graphene, Phys. Rev. Lett. **123**, 216803 (2019).

[17] Y.-B. Yang, K. Li, L.-M. Duan, and Y. Xu, Higher-order topological Anderson insulators, Phys. Rev. B **103**, 085408 (2021).

[18] R. Chen, C.-Z. Chen, J.-H. Gao, B. Zhou, and D.-H. Xu, Higher-order topological insulators in quasicrystals, Phys. Rev. Lett. **124**, 036803 (2020).

[19] A. Matsugatani and H. Watanabe, Connecting higher-order topological insulators to lower-dimensional topological insulators, Phys. Rev. B **98**, 205129 (2018).

[20] M. Ezawa, Higher-order topological insulators and semimetals on the breathing kagome and pyrochlore lattices, Phys. Rev. Lett. **120**, 026801 (2018).

[21] C.-H. Hsu, P. Stano, J. Klinovaja, and D. Loss, Majorana Kramers pairs in higher-order topological insulators, Phys. Rev. Lett. **121**, 196801 (2018).

[22] S. Franca, J. van den Brink, and I. C. Fulga, An anomalous higher-order topological insulator, Phys. Rev. B **98**, 201114(R) (2018).

[23] E. Khalaf, Higher-order topological insulators and superconductors protected by inversion symmetry, Phys. Rev. B **97**, 205136 (2018).

[24] H. Fan, B. Xia, L. Tong, S. Zheng, and D. Yu, Elastic higher-order topological insulator with topologically protected corner states, Phys. Rev. Lett. **122**, 204301 (2019).

[25] Y. Wu, H. Jiang, J. Liu, H. Liu, and X. C. Xie, Non-Abelian braiding of Dirac fermionic modes using topological corner states in higher-order topological insulator, Phys. Rev. Lett. **125**, 036801 (2020).

[26] Y. You, T. Devakul, F. J. Burnell, and T. Neupert, Higher-order symmetry-protected topological states for interacting bosons and fermions, Phys. Rev. B **98**, 235102 (2018).

[27] L. Trifunovic and P. W. Brouwer, Higher-order bulk-boundary correspondence for topological crystalline phases, Phys. Rev. X **9**, 011012 (2019).

[28] C.-A. Li, S.-B. Zhang, J. Li, and B. Trauzettel, Higher-order Fabry-Pérot interferometer from topological hinge states, Phys. Rev. Lett. **127**, 026803 (2021).

[29] S. A. A. Ghorashi, T. L. Hughes, and E. Rossi, Vortex and surface phase transitions in superconducting higher-order topological insulators, Phys. Rev. Lett. **125**, 037001 (2020).

[30] N. Shumiya, M. S. Hossain, J.-X. Yin, Z. Wang, M. Litskevich, C. Yoon, Y. Li, Y. Yang, Y.-X. Jiang, G. Cheng *et al.*, Evidence of a room-temperature quantum spin Hall edge state in a higher-order topological insulator, Nat. Mater. **21**, 1111 (2022).

[31] L. Fu, C. L. Kane, and E. J. Mele, Topological insulators in three dimensions, Phys. Rev. Lett. **98**, 106803 (2007).

[32] J. E. Moore and L. Balents, Topological invariants of time-reversal-invariant band structures, Phys. Rev. B **75**, 121306(R) (2007).

[33] L. Fu and C. L. Kane, Topological insulators with inversion symmetry, Phys. Rev. B **76**, 045302 (2007).

[34] D. Hsieh, D. Qian, L. Wray, Y. Xia, Y. S. Hor, R. J. Cava, and M. Z. Hasan, A topological Dirac insulator in a quantum spin Hall phase, Nature (London) **452**, 970 (2008).

[35] M. Z. Hasan and C. L. Kane, Colloquium: Topological insulators, Rev. Mod. Phys. **82**, 3045 (2010).

[36] X.-L. Qi and S.-C. Zhang, Topological insulators and superconductors, Rev. Mod. Phys. **83**, 1057 (2011).

[37] C. L. Kane and E. J. Mele, Quantum spin Hall effect in graphene, Phys. Rev. Lett. **95**, 226801 (2005).

[38] A. P. Schnyder, S. Ryu, A. Furusaki, and A. W. W. Ludwig, Classification of topological insulators and superconductors in three spatial dimensions, Phys. Rev. B **78**, 195125 (2008).

[39] C. L. Kane and E. J. Mele, Z_2 topological order and the quantum spin Hall effect, Phys. Rev. Lett. **95**, 146802 (2005).

[40] B. A. Bernevig, T. L. Hughes, and S.-C. Zhang, Quantum spin Hall effect and topological phase transition in HgTe quantum wells, Science **314**, 1757 (2006).

[41] Q. Wei, X. Zhang, W. Deng, J. Lu, X. Huang, M. Yan, G. Chen, Z. Liu, and S. Jia, Higher-order topological semimetal in acoustic crystals, Nat. Mater. **20**, 812 (2021).

[42] X. Ni, M. Weiner, A. Alu, and A. B. Khanikaev, Observation of higher-order topological acoustic states protected by generalized chiral symmetry, Nat. Mater. **18**, 113 (2019).

[43] Y. Qi, C. Qiu, M. Xiao, H. He, M. Ke, and Z. Liu, Acoustic realization of quadrupole topological insulators, Phys. Rev. Lett. **124**, 206601 (2020).

[44] S. Mittal, V. V. Orre, G. Zhu, M. A. Gorlach, A. Poddubny, and M. Hafezi, Photonic quadrupole topological phases, Nat. Photon. **13**, 692 (2019).

[45] A. El Hassan, F. K. Kunst, A. Moritz, G. Andler, E. J. Bergholtz, and M. Bourennane, Corner states of light in photonic waveguides, Nat. Photon. **13**, 697 (2019).

[46] M. Serra-Garcia, V. Peri, R. Süsstrunk, O. R. Bilal, T. Larsen, L. G. Villanueva, and S. D. Huber, Observation of a phononic quadrupole topological insulator, Nature (London) **555**, 342 (2018).

[47] F. Li, X. Huang, J. Lu, J. Ma, and Z. Liu, Weyl points and Fermi arcs in a chiral phononic crystal, Nat. Phys. **14**, 30 (2018).

[48] J. Bao, D. Zou, W. Zhang, W. He, H. Sun, and X. Zhang, Topo-electrical circuit octupole insulator with topologically protected corner states, Phys. Rev. B **100**, 201406(R) (2019).

[49] S. Imhof, C. Berger, F. Bayer, J. Brehm, L. W. Molenkamp, T. Kiessling, F. Schindler, C. H. Lee, M. Greiter, T. Neupert *et al.*, Topolectrical-circuit realization of topological corner modes, Nat. Phys. **14**, 925 (2018).

[50] Y. S. Hou, J. W. Kim, and R. Q. Wu, Axion insulator state in ferromagnetically ordered $CrI_3/Bi_2Se_3/MnBi_2Se_4$ heterostructures, Phys. Rev. B **101**, 121401(R) (2020).

[51] R. X. Zhang, F. Wu, and S. Das Sarma, Möbius insulator and higher-order topology in $MnBi_{2n}Te_{3n+1}$, Phys. Rev. Lett. **124**, 136407 (2020).

[52] C. Hu, K. N. Gordon, P. Liu, J. Liu, X. Zhou, P. Hao, D. Narayan, E. Emmanouilidou, H. Sun, Y. Liu *et al.*, A van der Waals antiferromagnetic topological insulator with weak interlayer magnetic coupling, Nat. Commun. **11**, 97 (2020).

[53] Y. Xu, Z. Song, Z. Wang, H. Weng, and X. Dai, Higher-order topology of the axion insulator $EuIn_2As_2$, Phys. Rev. Lett. **122**, 256402 (2019).

[54] H. Li, S.-Y. Gao, S.-F. Duan, Y.-F. Xu, K.-J. Zhu, S.-J. Tian, J.-C. Gao, W.-H. Fan, Z.-C. Rao, J.-R. Huang *et al.*, Dirac surface states in intrinsic magnetic topological insulators $EuSn_2As_2$ and $MnBi_{2n}Te_{3n+1}$, Phys. Rev. X **9**, 041039 (2019).

[55] C. Yue, Y. Xu, Z. Song, H. Weng, Y.-M. Lu, C. Fang, and X. Dai, Symmetry-enforced chiral hinge states and surface quantum anomalous Hall effect in the magnetic axion insulator $Bi_{2-x}Sm_xSe_3$, Nat. Phys. **15**, 577 (2019).

[56] M. König, S. Wiedmann, C. Brüne, A. Roth, H. Buhmann, L. W. Molenkamp, X.-L. Qi, and S.-C. Zhang, Quantum spin Hall insulator state in HgTe quantum wells, Science **318**, 766 (2007).

[57] B. Zhou, H.-Z. Lu, R.-L. Chu, S.-Q. Shen, and Q. Niu, Finite size effects on helical edge states in a quantum spin-Hall system, Phys. Rev. Lett. **101**, 246807 (2008).

[58] Y. Zhang, K. He, C.-Z. Chang, C.-L. Song, L.-L. Wang, X. Chen, J.-F. Jia, Z. Fang, X. Dai, W.-Y. Shan *et al.*, Crossover of the three-dimensional topological insulator Bi_2Se_3 to the two-dimensional limit, Nat. Phys. **6**, 584 (2010).

[59] C.-X. Liu, H. J. Zhang, B. Yan, X.-L. Qi, T. Frauenheim, X. Dai, Z. Fang, and S.-C. Zhang, Oscillatory crossover from two-dimensional to three-dimensional topological insulators, Phys. Rev. B **81**, 041307(R) (2010).

[60] R. Chen and B. Zhou, Finite size effects on the helical edge states on the Lieb lattice, Chin. Phys. B **25**, 067204 (2016).

[61] H. Xia, Y. Li, M. Cai, L. Qin, N. Zou, L. Peng, W. Duan, Y. Xu, W. Zhang, and Y.-S. Fu, Dimensional crossover and topological phase transition in Dirac semimetal Na$_3$Bi films, ACS Nano **13**, 9647 (2019).

[62] L. Muechler, E. Liu, J. Gayles, Q. Xu, C. Felser, and Y. Sun, Emerging chiral edge states from the confinement of a magnetic Weyl semimetal in Co$_3$Sn$_2$S$_2$, Phys. Rev. B **101**, 115106 (2020).

[63] R. Chen, C.-Z. Chen, B. Zhou, and D.-H. Xu, Finite-size effects in non-Hermitian topological systems, Phys. Rev. B **99**, 155431 (2019).

[64] A. C. Lygo, B. Guo, A. Rashidi, V. Huang, P. Cuadros-Romero, and S. Stemmer, Two-dimensional topological insulator state in cadmium arsenide thin films, Phys. Rev. Lett. **130**, 046201 (2023).

[65] H.-Z. Lu, W.-Y. Shan, W. Yao, Q. Niu, and S.-Q. Shen, Massive Dirac fermions and spin physics in an ultrathin film of topological insulator, Phys. Rev. B **81**, 115407 (2010).

[66] See Supplemental Material at http://link.aps.org/supplemental/10.1103/PhysRevB.108.165427 for (Sec. SI) Model and symmetries, (Sec. SII) general surface states and associated energy dispersion, (Sec. SIII) semi-infinity results on x-direction, (Sec. SV) finite-sized results on x-direction, (Sec. SV) finite-sized solutions on z-direction and (Sec. SVI) effective model for z-direction, which includes Refs. [3,5,65,67].

[67] W.-Y. Shan, H.-Z. Lu, and S.-Q. Shen, Effective continuous model for surface states and thin films of three-dimensional topological insulators, New J. Phys. **12**, 043048 (2010).

[68] H.-P. Sun, C. M. Wang, S.-B. Zhang, R. Chen, Y. Zhao, C. Liu, Q. Liu, C. Chen, H.-Z. Lu, and X. C. Xie, Analytical solution for the surface states of the antiferromagnetic topological insulator MnBi$_2$Te$_4$, Phys. Rev. B **102**, 241406(R) (2020).

[69] H.-P. Sun, C.-A. Li, S.-J. Choi, S.-B. Zhang, H.-Z. Lu, and B. Trauzettel, Magnetic topological transistor exploiting layer-selective transport, Phys. Rev. Res. **5**, 013179 (2023).

[70] S.-Q. Shen, *Topological Insulators: Dirac Equation in Condensed Matter* (Springer, New York, 2017), Vol. 174.

[71] X.-L. Qi, Y.-S. Wu, and S.-C. Zhang, Topological quantization of the spin Hall effect in two-dimensional paramagnetic semiconductors, Phys. Rev. B **74**, 085308 (2006).

[72] A. H. MacDonald and P. Středa, Quantized Hall effect and edge currents, Phys. Rev. B **29**, 1616 (1984).

[73] B. I. Halperin, Quantized Hall conductance, current-carrying edge states, and the existence of extended states in a two-dimensional disordered potential, Phys. Rev. B **25**, 2185 (1982).

[74] Considering a quantum Hall slab, owing to the external magnetic field the symmetric center of the energy band is not zero. Therefore, on the Fermi surface, the edges states distributed on opposite edges possess different momentum, which causes their uncoupling.

[75] B. J. Wieder, Z. Wang, J. Cano, X. Dai, L. M. Schoop, B. Bradlyn, and B. A. Bernevig, Strong and fragile topological Dirac semimetals with higher-order Fermi arcs, Nat. Commun. **11**, 627 (2020).

[76] X.-L. Du, R. Chen, R. Wang, and D.-H. Xu, Weyl nodes with higher-order topology in an optically driven nodal-line semimetal, Phys. Rev. B **105**, L081102 (2022).

[77] L. Luo, H.-X. Wang, Z.-K. Lin, B. Jiang, Y. Wu, F. Li, and J.-H. Jiang, Observation of a phononic higher-order Weyl semimetal, Nat. Mater. **20**, 794 (2021).

[78] H.-X. Wang, Z.-K. Lin, B. Jiang, G.-Y. Guo, and J.-H. Jiang, Higher-order Weyl semimetals, Phys. Rev. Lett. **125**, 146401 (2020).

[79] Z.-M. Wang, R. Wang, J.-H. Sun, T.-Y. Chen, and D.-H. Xu, Floquet Weyl semimetal phases in light-irradiated higher-order topological Dirac semimetals, Phys. Rev. B **107**, L121407 (2023).

[80] M. Lin and T. L. Hughes, Topological quadrupolar semimetals, Phys. Rev. B **98**, 241103(R) (2018).

[81] Z. Wang, B. J. Wieder, J. Li, B. Yan, and B. A. Bernevig, Higher-order topology, monopole nodal lines, and the origin of large Fermi arcs in transition metal dichalcogenides XTe$_2$ (X = Mo, W), Phys. Rev. Lett. **123**, 186401 (2019).

[82] D. Călugăru, V. Juričić, and B. Roy, Higher-order topological phases: A general principle of construction, Phys. Rev. B **99**, 041301(R) (2019).

[83] K. Wang, J.-X. Dai, L. B. Shao, S. A. Yang, and Y. X. Zhao, Boundary criticality of $\mathcal{PT}$-invariant topology and second-order nodal-line semimetals, Phys. Rev. Lett. **125**, 126403 (2020).

[84] S. K. Chong, L. Liu, K. Watanabe, T. Taniguchi, T. D. Sparks, F. Liu, and V. V. Deshpande, Emergent helical edge states in a hybridized three-dimensional topological insulator, Nat. Commun. **13**, 6386 (2022).

[85] Y. Xu, G. Jiang, I. Miotkowski, R. R. Biswas, and Y. P. Chen, Tuning insulator-semimetal transitions in 3D topological insulator thin films by intersurface hybridization and in-plane magnetic fields, Phys. Rev. Lett. **123**, 207701 (2019).